A Magnetorheologically Damped Compliant Foot for a Legged Robotic Application

Esa Kostamo[1]
Aalto University School of Engineering, Sähkömiehentie 4, 02150 Espoo Finland
email:esa.kostamo@aalto.fi
Michele Focchi [2]
Department of Advanced Robotics, Istituto Italiano di Tecnologia,
via Morego, 30, 16163 Genova, Italy
Emanuele Guglielmino [3]
Department of Advanced Robotics, Istituto Italiano di Tecnologia,
via Morego, 30, 16163 Genova, Italy
Jari Kostamo [4]
Aalto University School of Engineering, Sähkömiehentie 4, 02150 Espoo Finland
Claudio Semini [5]
Department of Advanced Robotics, Istituto Italiano di Tecnologia,
via Morego, 30, 16163 Genova, Italy
Jonas Buchli [6]
Institute of Robotics and Intelligent Systems, ETH Zurich, Tannenstr. 3,
8092 Zürich Switzerland
Matti Pietola [7]
Aalto University School of Engineering, Otakaari 4, 02150 Espoo Finland
Darwin Caldwell [8]
Department of Advanced Robotics, Istituto Italiano di Tecnologia,
via Morego, 30, 16163 Genova, Italy

ABSTRACT

The aim of this work is to enhance the controllability and the balance of a legged robot by improving the traction between the foot tip and the ground, since the stability of the robot can be influenced only during the phase when the foot is touching the ground. Within the framework of the hydraulically actuated quadruped robot, called HyQ, this paper presents an innovative solution for bouncing reduction between a robotic leg and the ground by means of a semi-active compliant foot. The compliant foot is custom-designed for quadruped walking robots and it consists of a linear spring and a magnetorheological damper. By utilizing magnetorheological technology in the damper element, the damping coefficient of the compliant foot can be altered in a wide range without any additional moving parts.
The content of this paper is twofold. In the first part the design, the prototype and a model of the semi-active compliant foot are presented, and the performances of the magnetorheological damper are experimentally studied in quasi-static and dynamic cases. Based on the quasi-static measurements the damping force can be controlled in a range from 15 N to 310 N. From the frequency response measurements it can be analyzed that the generated damping force has a bandwidth higher than 100 Hz.
The second part of this paper presents an online stiffness identification algorithm and a mathematical model of the HyQ leg. Using this model the relevant physical parameters are identified. A critical damping control law is proposed and implemented in order to demonstrate the effectiveness of the device that makes use of smart materials. Further on, drop-down experiments have been carried out to assess the performance of the proposed control law in terms of bounce

reduction and settling time. In the test setup the HyQ leg was attached to a vertically sliding test setup and in the leg the compliant foot was mounted to the lower limb segment. With the total mass of 7 kg the robotic leg was dropped from the heights of 0.1 m, 0.2 m and 0.3 m. In the results it will be demonstrated that by real time control of the damping force 98% bounce reduction with settling time of 170 ms can be achieved.
Keywords: magnetorheological, damping, bouncing reduction, energy dissipation, semi-active, robotic leg

1 INTRODUCTION

In industrial robotic applications engineers have traditionally striven to maximize the stiffness of the robotic arms. This kind of trend is well justified since an increment in stiffness improves the precision, stability and bandwidth of position-control without compromising the stability of the system. However in these applications the operating environment of the robot is precisely known and the mechanical design and the controller parameters can be finely tuned to meet the design target.

Another class of robotic machines is bio-mimetic robots. By definition, bio-mimetic robots mimic the structure and movement of humans and animals [1]. Such robots are often designed to operate in unstructured environment, where joint compliance plays a major role [2]. In particular compliant legged robots have the potential to walk or run through uneven and possibly unknown environments.

To achieve robust robotic legged locomotion over difficult terrains, different control approaches are required than just high gain position control. Such robots exhibit a very stiff disturbance rejection behavior and are therefore not well suited to deal with unstructured environments as presented by the real world outside the laboratory. In these applications it is better to use force control algorithm, because the robot needs to adapt to changing environments or to react smoothly to unexpected obstacles and forces. A lot of approaches can be implemented to control interaction forces [1] that might be good candidates to fulfill the requirements. On the other hand the performance of these techniques is limited by the actuator dynamics [1]. Bandwidth limitation creates difficulties in damping out impact forces and abrupt contacts with the environment. In general a force feedback in which a rigid body and a stiff load cell are combined has several shortcomings. In a load cell even a small movement causes high feedback force value resulting in a strong control action in a high-gain controller. This could result in instability and chatter when the robot enters in contact with a stiff environment. To remove the chatter lower gain values should be used causing a slower response of the robotic actuator.

To overcome this challenge a lot of effort has been invested in studying different kinds of passive compliant actuators for robotic applications to decouple the robot inertia from the environment. By using an elastic coupling between the robotic actuator and the target several benefits compared to stiff structure can be listed as follows [3]:

- Improved shock tolerance. In case of unexpected collision the shock forces can be damped without breaking the drive train.
- Improved force control stability. In contact with hard surface chatter is eliminated since a relatively large spring deflection is needed to exert a force.
- Ability to store and release energy in passive elements.
- Reduced force fidelity requirements of the components. Less expensive actuators and gears can be used because it is the motor shaft's position, not its output torque that is responsible for the generation of the load force.

To this day many variations and concepts of elastic or compliant actuators have been presented. In their study Pratt et al. introduced a concept of Series Elastic Actuators (SEA) that essentially consists of a linear spring in series with a stiff actuator [4]. The SEA meets the benefits listed above

but the compliance of the actuator is determined by the spring constant and therefore cannot be adjusted during the operation. The ability to change the joint stiffness is desirable in robotic applications because this enables to change the dynamics of a robot. The concept of Variable Stiffness Actuator (VSA) was described by Tonietti et al. [5]. Their mechanism is based on a spring – pulley – belt system which has more complex non – linearity of the output force compared to many other designs. On the other hand more compact size of the VSA can be considered as an advantage. Another approach to realize an elastic actuator is the Actuator with Mechanically Adjustable Series Compliance (AMASC) developed by Hurst et al. [6]. The complex mechanism of the AMASC is based on a multiple number of pulleys and cables but the advantage is that only one actuator is needed to control the compliance or equilibrium position.

Perhaps the most organic muscle imitating actuator can be carried out by pneumatic artificial muscles (PAM). The pressurization of the PAM expands the actuator radially creating an axial force. The pressurized air inside the PAM makes the actuator inherently compliant, behaving in a tendon-like fashion. The most well-known PAM design is the McKibben muscle [7]. The braided mesh structure of the muscle creates high stiffness in the axial direction but also notable hysteresis to the force output of the actuator that causes problems to control. In their study Verrelst et al. implemented pleated pneumatic artificial muscles in the biped robot Lucy [8]. With pleated design the hysteresis in the force output can be significantly reduced enabling more accurate force control. Even more precise reproduction of a musclotendon-like actuator was proposed by Klute et al. [9]. In their study two pneumatic artificial muscles were used as a contracting elements and a passive hydraulic damper was mounted parallel with the muscles in order to attain desired force-velocity properties for the actuator. As an artificial tendon two linear springs were utilized in series with the pneumatic muscles and the damper. Experimental results showed the actuator – damper – tendon system behaved in a muscle – and tendon – like manner.

In general much less effort has been invested in studying damping in robotic actuator systems. In a study by Wait and Goldfarb a pneumatic actuator was supplemented with a mechanical damper in order to improve the performance and stability of the system [10]. The authors concluded that by adding passive damping the gain margin, tracking accuracy and disturbance rejection of closed – loop controlled pneumatic servo actuators can be significantly increased. Further on the combination of pneumatic actuator and hydraulic damper was studied in a quadruped walking robot by Wait and Goldfarb [11]. The control of the robot's joint motions incorporated open-loop damping into the actuation and use of a stance/ swing gain scheduler in the joint position controller. As a result it was experimentally demonstrated that stable walking without significant oscillations of the body or legs can be attained by the developed joint trajectories and damped pneumatic actuators.

In comparison to series elastic actuators Chew et al. proposed a concept of series damper actuator (SDA) [12]. In their study the experimental setup consisted of an electric motor, rotational magnetorheological damper (Lord MRB-2107-3), load and necessary sensors to measure the torque and angular velocities before and after the magnetorheological damper. As an advantage the damping coefficient of the system can be continuously controlled that enable high torque fidelity at both high and low torque ranges. The SDA has also inherent impact absorption property that is very important for walking robots, haptic devices or robot manipulators. The main disadvantage of the SDA is also related to its energy dissipation property. The SDA application can only dissipate energy from the system since there is no energy conserving elastic component. By the experimental results it was demonstrated that the SDA can be controlled to have linear torque versus velocity relationship with varying damping coefficient.

The variable physical damping actuator (VPDA) for robotic applications was also studied by Laffranchi et al. [13]. In their study the rotational VPDA unit consisted of piezoelectric actuated friction damper and a passive torsion spring element coupled in parallel to the damper. The advantages compared to other semi-active damping technologies have been listed such as compact

and light weight structure, cleanliness and simple mechanical design. By the experimental results it was demonstrated that the VPDA can be an effective mean for the damping of the oscillations in rotational robotic joints. A control law for VPDA was proposed showing that different damping ratios could be replicated with good fidelity.

The objective of this study is to improve the contact of the foot of a legged robot on the ground by combining a magnetorheological (MR) damping element with a spring to create a semi-active compliant robotic foot. The main drawback of passive compliant elements is that chatter/bouncing between the foot tip and the ground can occur and thus traction can be temporarily lost. The energy stored in a spring, that can generate bouncing, can be dissipated by using a passive damping element but on the other hand a passive damper would perform a critically damped response only for a particular pair of robot masses and spring constants. In the framework of the balance control of the quadruped robot HyQ [14], [15], reduced bouncing and improved ground contact are crucial since robot posture can be adjusted only during the stance. In some operating conditions it can be also beneficial, from an energy efficiency point of view, to have as low damping coefficient as possible. Therefore it is worth investigating the feasibility of using controlled semi-active damping [16] in order to reduce bouncing induced on the robot by the impact forces at touch-down.

By utilizing the MR technology the damping force of the novel compliant foot presented in this paper can be controlled in a range that goes from ten Newtons up to hundreds of Newtons with a bandwidth of 100 Hz. The fast response of the prototype MR damper enables a real time control of the damping force and therefore appropriate control algorithms can be activated during the stance phase, which in normal trotting for HyQ usually varies in a range of 100-300 ms depending on the gait parameters. By applying different control algorithms the damper can emulate the operation of a conventional viscous damper with controllable damping factor, a negative spring, a constant friction force or any combination thereof.

In this paper Sec. 2 gives a brief introduction to magnetorheological fluids and presents the design and functional components of the magnetorheological compliant foot. In Sec. 3 the magnetic properties of the MR damper are studied with a finite element model and a third order polynomial model is proposed to estimate the quasi-static characteristics of the MR damper. In Sec. 4 the performance of the MR damper is assessed in static and dynamic cases and the quasi-static model of the damper is compared with experimental data. Section 5 gives a description of the prototype of the robotic leg that is used for the implementation of the bouncing control algorithms. Section 6 briefly describes how to translate the stiffness from the end-effector space to the joint space, which is required for the following sections. Section 7 describes a simplified mathematical model of the dynamics of the HyQ leg in the vertical direction and presents a methodology to estimate the stiffness during the locomotion (on-line). In Sec. 8 a critically damped control law for bounce reduction is presented and finally Sec. 9 shows experimental results that show the capability of the MR damped to reduce the bouncing in drop-down experiments of the leg. Finally, Sections 10 address the conclusions.

2 MAGNETORHEOLOGICAL COMPLIANT FOOT

This section introduces magnetorheological fluids and their operational principle and the construction of the magnetorheological compliant foot that was developed and manufactured for this study.

2.1 Magnetorheological fluids

Magnetorheological fluids belong to the group of smart materials whose characteristic properties can be altered by an external magnetic field. MR fluids essentially consist of micron-sized magnetisable particles in a low viscosity carrier fluid. Small amount of additives and surfactant may also be mixed into the fluid to reduce sedimentation of the particles and therefore improve the stability of the fluid. The functional principle of the fluid is based on the alignment of the

ferromagnetic particles along the magnetic flux lines. The particle chains increase the yield stress of the fluid and by the applied magnetic field the fluid flow can be resisted or totally restricted. In short, the MR effect can be defined as a reversible change of the rheological properties of the MR fluid from free flowing Newtonian fluid to semi-solid Bingham-like material [17]. By utilizing this mechanism the characteristic properties of an MR device can be altered in a wide range without any moving or wearing parts.

MR fluids can be considered as an interesting technology for highly dynamic applications. In the literature it has been reported that the response time for the alignment of the particles in MR fluid is less than 0.5 ms [18]. It has also been shown that a damper in the range of kilo Newton damping force can be constructed to operate within a response time of 2 ms [19].

The MR fluid used in this study is the MRF-132DG by LORD Corporation. It is a hydrocarbon based fluid that has a high resistance to hard settling and is developed for energy dissipative applications. In Fig. 1a the magnetic field induced yield stress is plotted versus the magnetic field strength. According to the manufacturer, the fluid reaches its maximum yield stress of 48 kPa at a magnetic field strength of approximately 280 kA/m. The magnetization curve of the MRF-132DG, that is needed in the magnetic modeling of the device, is presented in Fig. 1b.

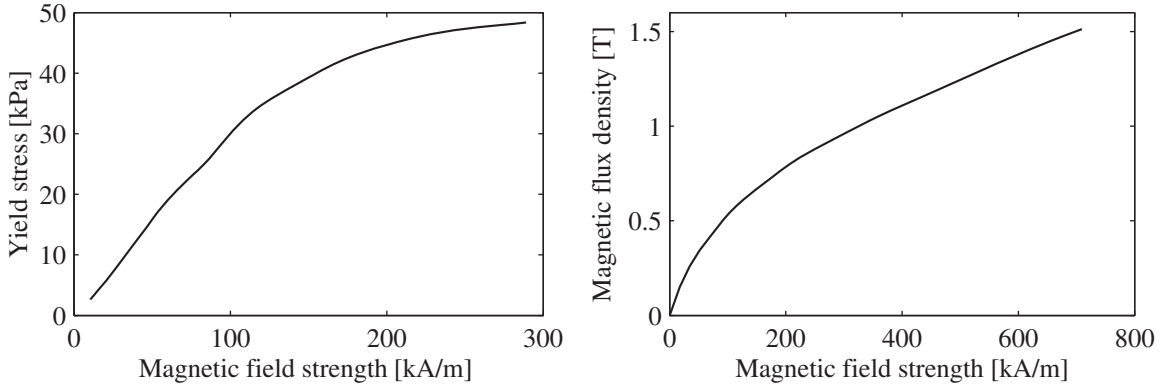

Fig. 1a, MRF-132DG yield stress as a function of magnetic field strength, Fig. 1b, MRF-132DG magnetization characteristic curve [20]

2.2 Construction of the magnetorheological compliant foot

The construction of the prototype magnetorheological compliant foot is presented in Fig. 2 with a CAD cross-section view in which the main functional components are numbered and pointed out. The end caps (4) and (12) are machined of aluminum and the material of the piston shaft (2) is a surface hardened steel guide bar. Magnetically active parts in the construction are the piston (10) and the cylinder (11) which are manufactured of magnetically soft iron. The coil around the piston is wound of 0.4 mm enameled copper wire.

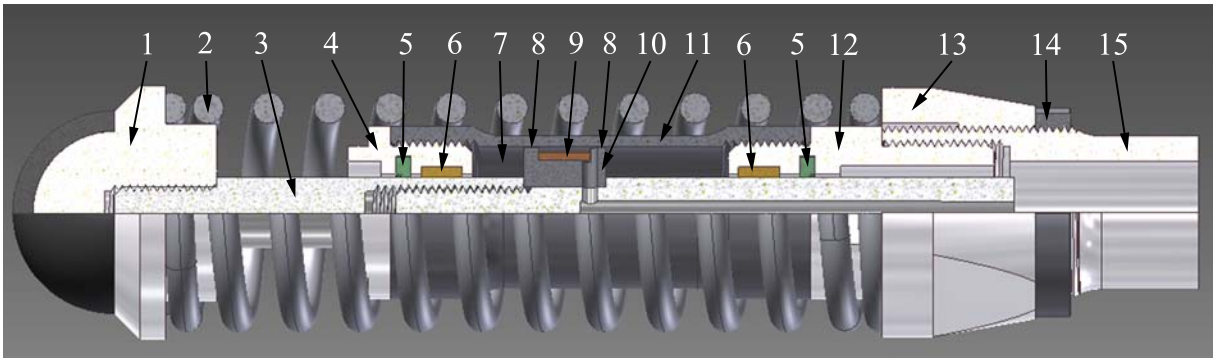

Fig. 2, CAD cross-section view of the MR foot. Numbered components: (1) rubber coated foot tip, (2) spring, (3) piston shaft, (4) lover end cap, (5) seal, (6) sliding bushing, (7) MR fluid, (8) MR fluid gap, (9) solenoid, (10) piston, (11) cylinder, (12) upper end

The MR compliant foot is assembled as shown in Fig. 2 and the remaining volume inside the cylinder is filled with magnetorheological fluid. The piston is manufactured to have one millimeter smaller diameter in relation to the inner diameter of the cylinder tube. This difference forms a 0.5 mm annular fluid gap between the piston and the cylinder which enables the MR fluid to flow from one side of the piston to the other when the compliant foot is compressed or extended. Since the hydraulic components of the damper are designed to be symmetric, no gas reservoir is needed to compensate the movement of the piston.
The solenoid around the piston is used to generate the magnetic field between the piston and the cylinder. When electric current is applied, magnetic flux circulates in-between the piston and the cylinder tube over two fluid gaps ((8) in Fig. 2) and induce the increase in the MR fluid's yield stress. This increase in yield stress restricts the fluid flow over the piston, generating pressure difference over the piston and consequently generating damping force when the piston rod is moved. Because the change in the fluid's rheological properties is completely reversible, the damping force can be continuously controlled by adjusting the electric current in the coil. The key parameters of the magnetorheological compliant foot are listed in Table 1.

Table 1, Key parameters of the magnetorheological compliant foot

Weight	1.1 kg
Total length	232 mm
Stroke	34 mm
Largest diameter	49 mm
Cylinder inner diameter	26 mm
Piston diameter	25 mm
Fluid gap	0,5 mm
Spring constant	15.8 N/mm
Number of Ampere turns in the coil	80
Max damping force (@4A electric current)	485 N
Operating bandwidth, -3dB limit	>100 Hz
Max input power	<4 W

3 MODEL OF THE MAGNETORHEOLOGICAL DAMPER

This section focuses on the modeling of the magnetorheological damper within the compliant foot. When formulating the model of the controllable damping force, the spring force is not taken into account in order to be purely able to focus on damping force generated by the semi-active damper.

3.1 Magnetic model of the magnetorheological damper

The magnetic properties of the MR damper were estimated by using Finite Element Method Magnetics (FEMM) software. In the FEMM software the nonlinear magnetic properties of the MR fluid (Fig. 1b) can be taken into account and the intensity of the magnetic field in the fluid gap can be estimated with different values of electric current. Since the light weight structure of the damper was one of the most essential design criteria, the thickness of the magnetically active parts, especially the thickness of the cylinder, needed to be optimized with respect to the maximum intensity of the magnetic field in the fluid and the total mass of the damper. From the magnetic performance point of view it was desired that the damper would have a linear response of the magnetic field up to a current of two amperes with 80 turns in the solenoid resulting in no saturation of the core material.

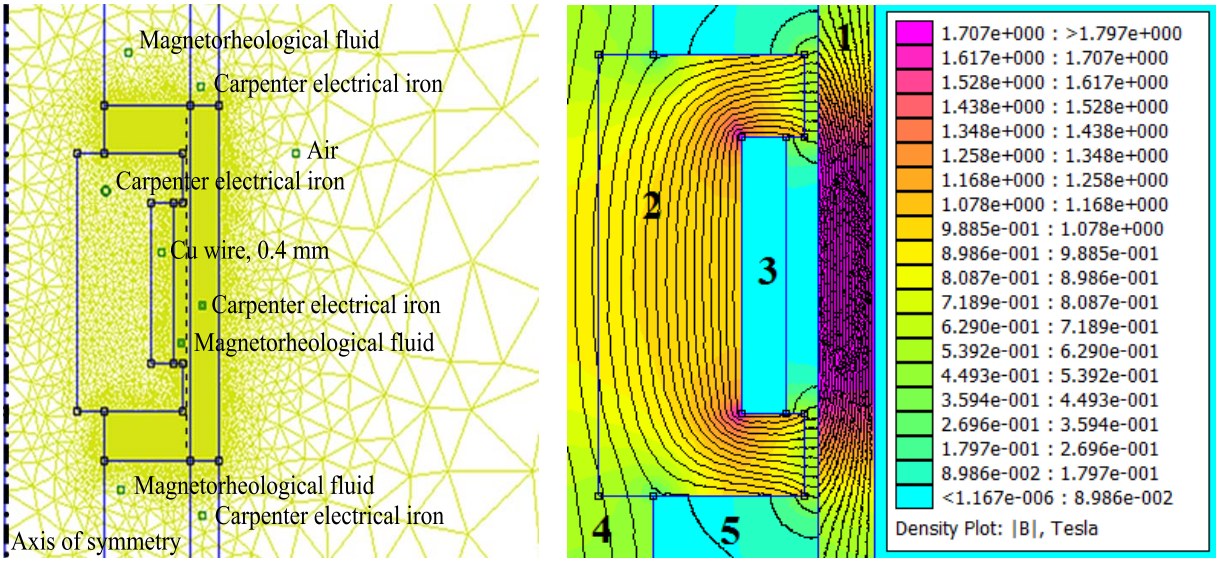

Fig. 3a, Close-up of the meshed FEMM model of the MR damper Fig. 3b, Solved model at electric current of 2 A. Numbered components: (1) cylinder, (2) piston, (3) solenoid, (4) piston shaft, (5) magnetorheological fluid.

The close-up of the meshed FEMM model of the MR damper is presented in Fig. 3a. The piston and the cylinder parts of the damper are made of Carpenter electrical iron having high magnetic saturation point. Its characteristic curve can be found from the material library of the software. The solenoid, in the middle of the piston, was manufactured of 0.4 mm enameled copper wire having 80 wire turns in total. Figure 3b presents the magnetic flux distribution of the solved model at electric current of 2 A.

The MR fluid volume and the cylinder part in Fig. 3a were divided by the horizontal lines from the both sides of the piston in order to be able to use finer mesh in the most active part of the model. Size of the triangular mesh in the MR fluid and cylinder part (between the horizontal lines) was set to 0.05 mm (average height of the element) and in the piston material the element with the size of 0.5 mm was used. The dashed line crossing through the MR fluid gaps illustrates a line along which the intensity of the magnetic field in the MR fluid has been analyzed.

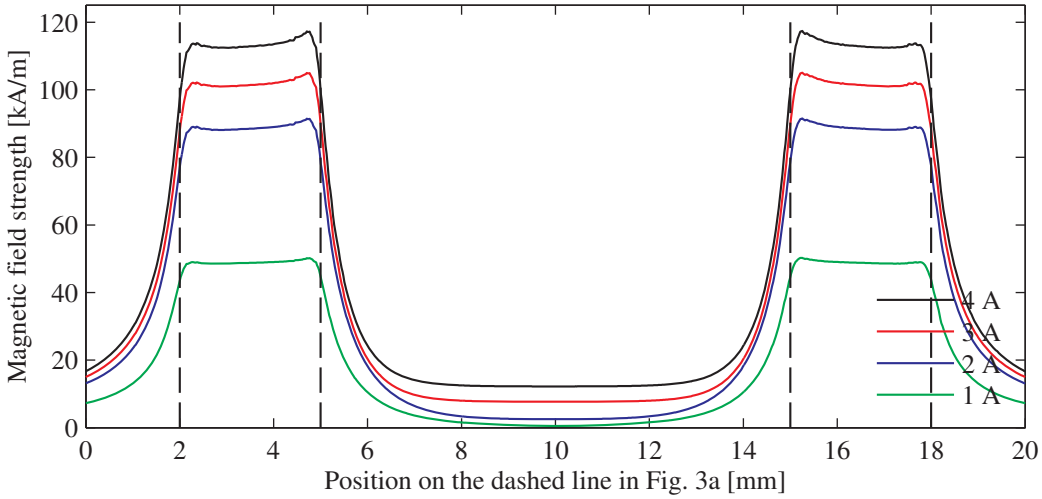

Fig. 4, Magnetic field strengths on the dashed line from the Fig. 3a FEMM model for different applied electric currents

Figure 4 shows the simulated responses of the magnetic field strength in the MR fluid gap at four different electric currents and the vertical dashed lines in are pointing out the edges of the MR fluid gaps ((8) in Fig. 2). From the simulated results it can be seen that the deviation of the magnetic field strength in the fluid gap is very flat and the increase in the magnetic field strength from zero to one

ampere and one to two amperes can be found approximately equal which indicates that no saturation occurs in the core material. With electric currents above 2 A the core parts of the damper begin to saturate, which can be seen as a decreased increment in the magnetic field strength when the electric current is increased by one ampere. It is also noteworthy that with electric currents above 2 A the magnetic flux begins to leak outside the MR fluid gap due to the saturation of the core material. In the middle of the piston, i.e. position between 5 mm and 15 mm, the magnetic field strength increases significantly at electric currents higher than 2 A, making also this area of the piston significant while simulating the static force response of the damper.

3.2 Quasi-static model

The magnetic field dependent characteristics of MR fluid is often modeled by using the Bingham plasticity equation. In this equation the total yield stress of the fluid is divided into magnetic field strength and passive viscosity dependent components. The general expression of the model is given by:

$$\begin{aligned} &\sigma = \sigma_0(H)\mathrm{sgn}(\dot{\gamma}) + \eta\gamma \\ &\dot{\gamma} = 0 \qquad |\sigma| < |\sigma_0| \end{aligned} \tag{1}$$

where σ is the total yield stress of the fluid, $\sigma_0(H)$ is the magnetic field dependent yield stress, $\dot{\gamma}$ is the shear rate and η is the field independent viscosity [17].

In the literature, many publications have focused on developing quasi-static models for controllable fluid dampers, in which it is assumed that: (a) the piston of the damper moves at a constant velocity; (b) MR fluid flow is fully developed; and (c) a Bingham plastic model can be employed to describe the MR fluid behavior [21]. In this study a third order polynomial model is used to describe the static characteristics of the MR damper. The model is slightly modified from the equation presented in [22] where the damping force is approximated as a function of the applied electric current and the velocity of the piston. In the original expression of the model the shape of the fluid gap is assumed to be rectangular, whereas in the case of the here presented MR compliant foot, the MR fluid flows through an annula-shaped fluid gap. The fluid gap in the MR damper is similar to the geometry depicted in Fig. 5.

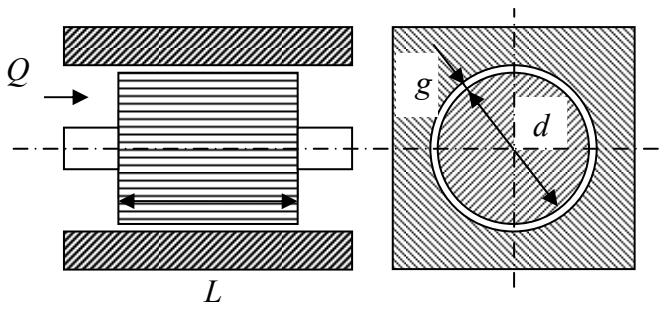

Fig. 5, Schematic of the fluid flow in an annular flow channel

The laminar Newtonian volume flow through an annular fluid gap with a pressure difference over the fluid gap can be written as:

$$Q = \frac{\pi d g^3}{12\eta L}(P_1 - P_2) \tag{2}$$

where d is the diameter of the piston in the fluid gap, g is the height of the fluid gap, L is the length of the fluid gap, P_1 is the pressure at the inlet side of the gap and P_2 is the pressure at the outlet side of the gap [23].

By replacing the magnetic field independent term in [22] with Eq. (2), the model for the developed MR damper becomes:

$$4\left(\frac{L}{g\Delta P_{tot}}\right)^3 \sigma_0(H)^3 - 3\left(\frac{L}{g\Delta P_{tot}}\right)\sigma_0(H) + \left(1 - \frac{12\eta LQ}{\pi d g^3 \Delta P_{tot}}\right) = 0 \quad (3)$$

where ΔP_{tot} is the total pressure difference over the fluid gap, and Q is the volume flow through the fluid gap.

The solution of this equation, with respect to the total pressure difference, can be found by numerical iteration. Of the three possible roots of this equation two are inadmissible leaving the largest positive root as the only possible solution with physical meaning.

Once the pressure difference at certain intensity of magnetic field and volume flow has been solved, it is straightforward to estimate the total force produced by the MR damper. By taking the friction force into account the total force F of the MR damper can be formulated as

$$F = \Delta P_{tot} A + F_\mu \quad (4)$$

where A is the effective piston area and F_μ is the friction force due to the seals and the sliding bushings.

The total pressure difference can be further analyzed as combination of the magnetic field dependent component ΔP_H and the post-yield plastic viscosity component ΔP_η of the fluid. Hence the total damping force can be decomposed into a magnetic field controllable force F_H and uncontrollable viscous F_η and friction forces.

The controllable force and the dynamic range are two important characteristics when defining the performance of an MR damper. The dynamic range is defined as the ratio between damper total force and the uncontrollable force F_{uc} and can be written as [21]:

$$D = \frac{F}{F_{uc}} = 1 + \frac{F_H}{F_\eta + F_\mu} \quad (5)$$

4 PERFORMANCE OF THE MAGNETORHEOLOGICAL DAMPER

This section presents a series of experimental results obtained with the MR damper. First the quasi-static performance of the MR damper is analyzed by using a stress-strain machine and the damper model Eq. (3) is validated by using this data. Then, the static performance of the damper is compared with the simulation model that combines magnetic properties of the damper, non-linearity of the MR fluid and the hydraulic model of the damper. The dynamic performance of the damper is studied by frequency response measurements in order to give insight into the maximum operating bandwidth of the prototype.

4.1 Quasi-static performance

The static performance of the MR damper was identified by using an Easydur MZ3 material testing device (stress-strain machine). In the experiment the magnetorheological compliant foot was mounted to the test setup without the spring in order to be able to study only the characteristic properties of the MR damper. In one measurement the damper was compressed and extended five times at a constant velocity and electric currents from 0 A to 2 A were supplied. From the measured results the constant velocity and the mean constant force were calculated resulting in five vertical force points in positive and negative directions for the static characteristic curves. This measuring procedure was repeated 60 times with different velocities in order to identify the static performance of the developed MR damper. The characteristic curves are presented in Fig. 6.

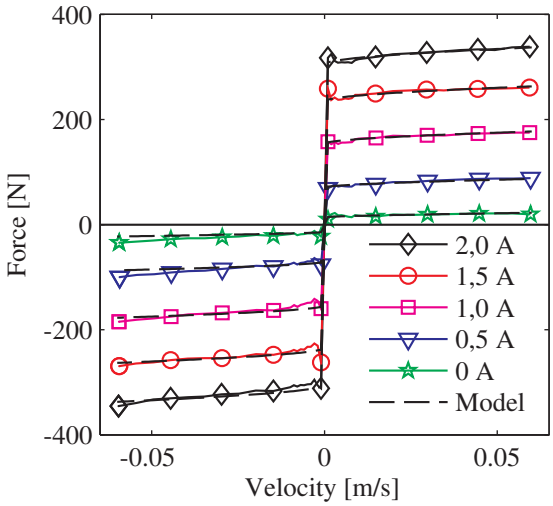

Fig. 6, Comparison of measured and simulated static force-velocity characteristic for different electric current inputs (0-2 A)

In Fig. 6 the zero speed force depends on the electric current induced yield stress of the MR fluid and the friction in the seals and sliding bushings. In addition the viscous forces will increase the measured total force as the damper begins to move. To simulate the quasi-static force response of the MR damper the model presented in Eq. (3) is compared with the measured data and presented with a dashed line. In the model the zero speed yield stresses are found by fitting linear curves to measured force data. All other parameters are based on the physical quantities of the damper. From Fig. 6 it can be seen that by using this model a good agreement can be found between measured results and simulated response.

Based on the results shown in Fig. 6, the dynamic range of the damper can be approximated by using Eq. (5). The ratio between the controllable and uncontrollable force at speed of 60 mm/s results in a value of 14.9 which can be considered as an indication of the controllability of the damping force in a wide range. In the development process of a MR damper application the dynamic range can be considered as a design parameter and can vary from 2 to 25 depending on the target of the application [24-26]. In this study the dynamic range is a trade-off between the maximal force, light weight structure and the fluid flow path design and can be considered as a successful value.

4.2 Friction force identification

The force response of the damper was also studied as a function of the applied electric current. In this measurement the damper was compressed at a constant velocity of 40 mm/s and electric currents with increment of 1 A up to 4 A were applied. The measured damping force is compared with the simulated response and the results are presented in Fig. 7. While analyzing the simulated results it is noteworthy that the results are completely (with exception of the friction forces) based on the theoretical analysis.

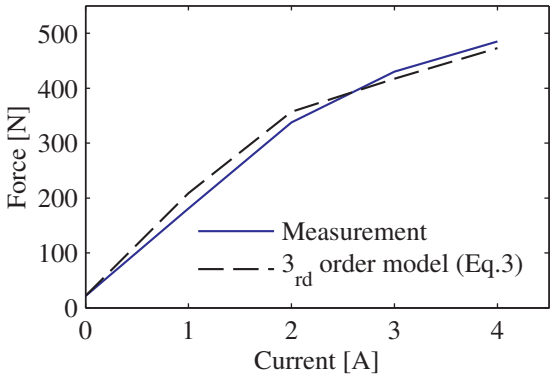

Fig. 7, Measured and simulated damping force responses of the magnetorheological damper of the compliant foot as a function of the electric current

The simulation of the damping force begins by creating a finite element (FE) model of the magnetic circuit of the MR device in which the non-linear permeability of the MR fluid can be taken into account (see Fig. 1b). Subsequently the yield stress of the MR fluid for different positions inside the fluid gap (and surroundings) can be estimated by combining the FE results of the magnetic field strength (Fig. 4) with the yield stress characteristic curve (see Fig. 1a) of the MR fluid. In the next step the yield stress results of the MR fluid in the fluid gap are combined with Eq. (3) and by integrating over the length of the piston, the total pressure difference over the piston can be estimated. In many cases sufficient accuracy is achieved when the pressure difference, caused by the MR effect, is integrated over the fluid gap(s) in which the MR fluid is activated. However in this analysis also the middle part of the piston (position range between 5 mm and 15 mm in Fig. 4) must be taken into account because the magnetic flux begins to spread outside of the MR fluid gap after saturation of the core parts. In this step one should also note that the height of the fluid gap is not constant but a function of the position over the length of the piston. In this study the correct fluid gap height was identified by measuring diameters of the manufactured piston at different positions.
After integration of the pressure difference over the piston, the total damping force can be calculated by Eq. (4).
The friction force in Eq. (4) was defined empirically. To study the friction force as a function of the applied electric current an identification cylinder was manufactured in which two pressure sensors can be mounted that measure the MR fluid pressures on both sides of the piston. By multiplying the pressure difference with the effective cross-section area of the piston, the damping force was calculated based on the pressure data and compared with the damping force measured with the force sensor of the test setup. By comparing these two results it was assumed that the difference between two force responses was caused by friction in the seals and the sliding bushings. After analysis of the force difference the following friction force function was obtained

$$F\mu(I) = 21.8[N/A] * I + 17[N] \tag{6}$$

where I is the applied electric current.
From Fig. 7 it can be seen that the model predicts the measured damping force with a satisfactory accuracy even if the damper operates in the range where the core parts begin to saturate (I > 2 A). In the operating range below 2 A the damping force increases linearly which was found to match well with the intended design criteria presented in Sec. 3.1.

4.3 Frequency response measurements

The dynamic performance of the MR damper was studied by frequency response measurements. In these measurements the damper was compressed and extended at a constant velocity of 30 mm/s and a sinusoidal current excitation was used. The peak-to-peak value of the current excitation was

2 A and the measured frequency band ranged from 2 Hz to 100 Hz with an increment of 2 Hz. The data sampling frequency was 1 kHz. The magnitude and phase curves of the frequency response measurement are presented in Fig. 8.

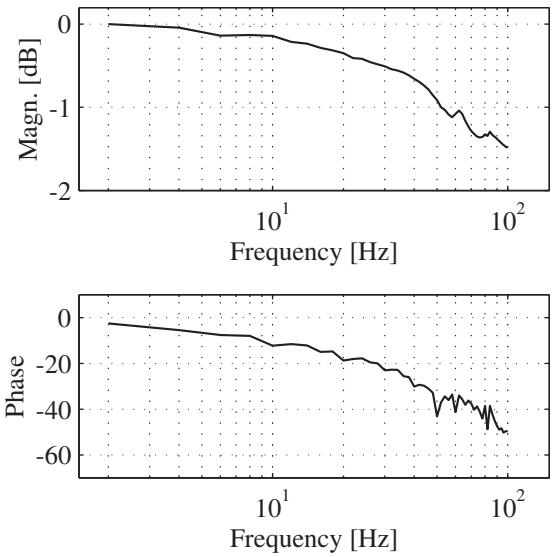

Fig. 8, Frequency response of the damping force of the magnetorheological damper

In the magnitude plot of Fig. 8, the 0 dB level can be estimated to correspond to a force of 340 N. The frequency response measurement was limited to 100 Hz, because it was estimated to be sufficient for this robotic application. The magnitude plot clearly shows that the -3 dB level is at a frequency level higher than 100 Hz. This can also be seen in the phase plot, where the phase lag is 50 degrees at 100 Hz. Based on these frequency response measurements it can be concluded that the MR damper maintains the controllability up to the desired frequency.

5 ROBOTIC LEG WITH THE MAGNETORHEOLOGICAL COMPLIANT FOOT

This section describes the robotic setup chosen to test the effectiveness of the MR damper. This consists in a robotic leg mounted on a vertical slider. The leg (henceforth HyQ leg) was designed for a hydraulically actuated quadruped robot called HyQ that is a scientific platform to study and develop locomotion of four-legged robots. The specifications of the leg and HyQ can be found in [14]. Only the 2 links in the sagittal plane are considered in this work. The MR damper was mounted into the lower part of the HyQ leg for the control application of this study, adding an additional prismatic joint to the leg.

The slider arrangement allows only vertical movement of the leg base and therefore allows studying the leg vertical bouncing dynamics. The experimental setup is presented in Fig. 9a with a functional description of the components. Figure 9b introduces a close-up view of the manufactured prototype of the compliant foot.

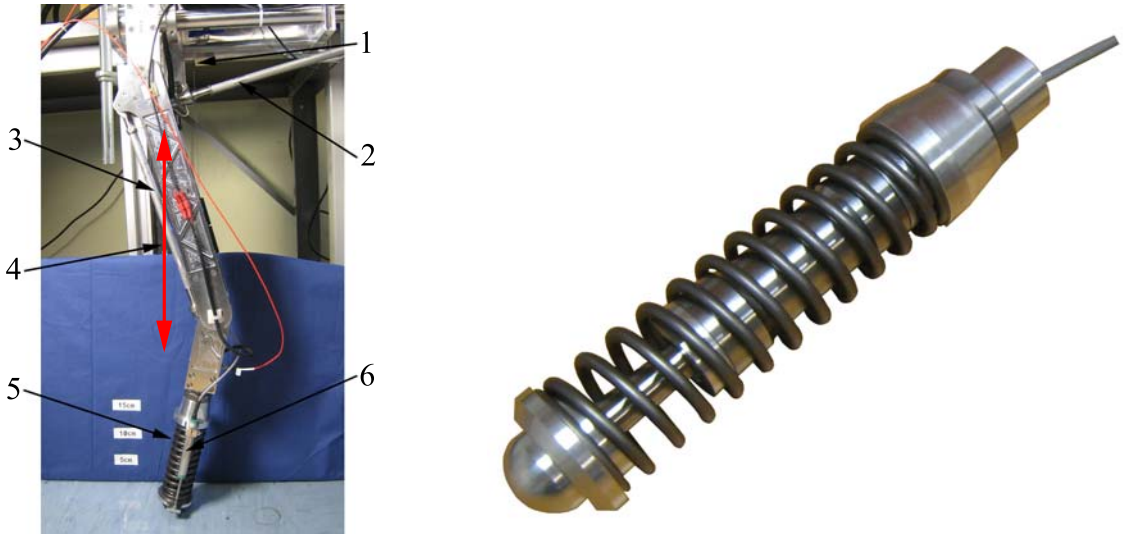

Fig. 9a, picture of the HyQ robotic leg with the magnetorheological compliant foot attached to a vertically sliding test setup: (1) slider position encoder, (2) hip support, (3) knee support, (4) slider guide, (5) magnetorheological compliant foot, (6) foot compression sensor. Fig. 9b, a close-up view of the magnetorheological compliant foot

The two joints of the robotic leg are normally actuated by two hydraulic cylinders but, in order to avoid the influence of the compliance of the oil and the hydraulic hoses, the hydraulic cylinders were replaced with stiff aluminum rods. These aluminum support rods were cut to certain length to obtain a configuration in which the hip angle equals to -12° and the knee angle equals to 24° (this corresponds to the orientation in which the foot-tip locates exactly under the hip axis). The definition of the hip and knee angles together with the definition of foot compression/extension can be found in Fig. 10b.
The spring displacement in the compliant foot was measured by a linear potentiometer (Burster 8709). An absolute encoder (Austrian MicroSystems AS5045), connected to a steel cable and pulley system, was used to define the vertical position of the slider. Ground reaction forces were recorded by means of a 3-axis force plate (Kistler 9260AA6). The sampling rates of the data acquisition and the frequency of the control loop were set to 1 kHz. The total leg mass (including the MR foot and the slider carriage) has a total weight of 7 kg. The spring in the compliant foot was chosen to have a spring constant of 15800 N/m. This value was selected to achieve maximum compression (0.035m) when the leg is dropped from a height of 0.3 m.

6 END-EFFECTOR STIFFNESS FOR THE LEG MECHANISM

The configuration of the leg (without aluminium rods) is defined in the joint space by two rotational degrees of freedom and one linear degree of freedom. The construction of the robotic leg is characterized by a serial chain of link with non-linear kinematics. The configuration of the leg may have a strong influence on the stiffness and the damping characteristics at the end-effector level.
In particular the damping force acts in the direction of the longitudinal axis of the lower leg segment (joint space), while the bouncing requirements are defined at the leg end-effector level (task space). Because of this it is necessary to describe how the stiffness of the leg can be mapped from the joint space to the task space.

6.1 Mapping from the joint space to the task space

The kinematics of the leg is shown in Fig. 10b. The joint space vector can be written as:

$$q = [q_1 \quad q_2 \quad q_3] \tag{7}$$

where the vector q is defined by the angular joint displacements of the hip (q_1), the angular joint displacements of the knee (q_2) and the linear displacement (q_3) in the compliant foot. The joints' stiffness tensor K_j is defined as the partial derivative of the joint torques τ with regard to the joint displacements q. Due to the absence of bi-articular joints K_j matrix will be diagonal. By expanding the torque derivative using the kineto-static duality [27] we obtain:

$$K_j = \frac{\partial \tau}{\partial q} = \frac{\partial \left(J^T f\right)}{\partial q} = \frac{\partial J^T}{\partial q} f + J^T \frac{\partial f}{\partial x}\frac{\partial x}{\partial q} = K_{geo} + J^T K_x J \tag{8}$$

where J is the Jacobian matrix from the joint space to the task space (foot) and f is the end-effector force vector from the foot to the environment. From the first component of Eq. 8 it can be seen that for a non-linear linkage the joint stiffness depends also on the force acting on the system. This component is called as geometric stiffness K_{geo} [28]. By rearranging Eq. 8 the end-effector stiffness tensor K_t can be obtained:

$$K_t = J^{+T}\left(K_j - K_{geo}\right)J^{+} \quad K_t = \begin{bmatrix} k_{xx} & k_{xy} \\ k_{yx} & k_{yy} \end{bmatrix} \tag{9}$$

As J is a rectangular 2x3 matrix it cannot be inverted. Therefore the Moore-Penrose pseudoinverse J^+ has been selected for the inversion. The overall expression has two components: K_j reflecting the stiffness of the joints and K_{geo} stemming from changes in Jacobian due to changes in the configuration [28]. Most of the times, the geometric stiffness can be neglected in relation to the other terms. Also in this study, since the hip/knee joints movement is fixed by aluminium rods, the only significant contribution to the leg compliance is due to the foot spring and the other two links can be considered as a unique rigid body. However when the rods will be replaced with pistons the first 2 terms on the diagonal of K_j matrix will represent the oil compressibility and the hose compliance in the hydraulic system.

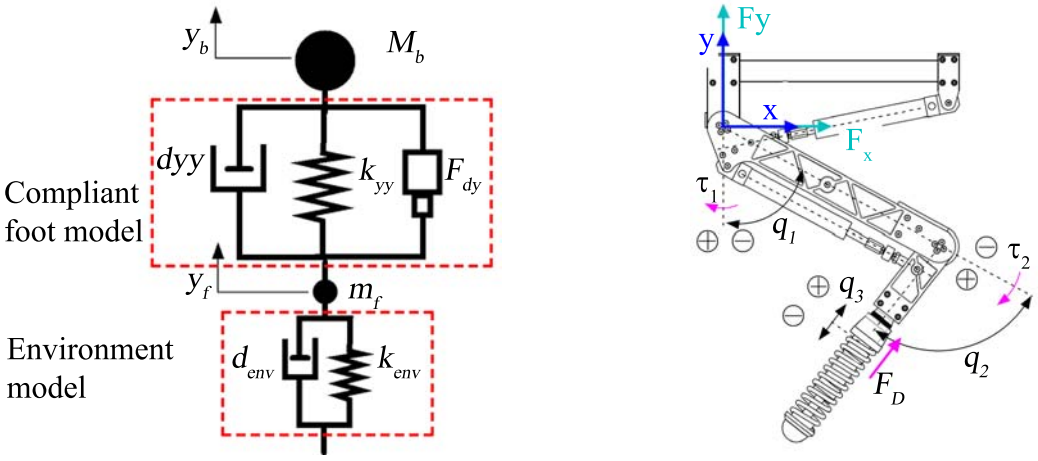

Fig. 10a, a spring- mass- damper equivalent of the robotic leg. Fig. 10b, joint and task space coordinates and forces

7 MATHEMATICAL MODELLING

During the stance phase the leg can be modelled as a spring-mass-damper system as illustrated in Fig. 10a. A lumped parameter mathematical model of the leg has been built up for the identification of the end-effector stiffness and the passive damping (e.g. due to joint friction) of the leg and for the

development of the control laws. In addition to the dynamic model of the leg a method for the online stiffness identification of the ground is also proposed in this section.

7.1 The dynamic model of the leg

The dynamic model of the leg is based on the estimation of the total forces on the different bodies of the leg and the projection of the forces in the y-direction of the end-effector. Because of the presence of the aluminium rods the masses of the links have been lumped into one mass (henceforth called body mass) m_b with sprung mass of 6.9 kg whereas the foot mass m_f is called by the mass of the tip of the foot located after the spring with unsprung mass of 0.1 kg. As a result two second order equations describe the bouncing vertical dynamics of the masses m_b and m_f:

$$\begin{cases} \ddot{y}_b = -g + \dfrac{1}{m_b}\left(-k_{yy}\left(y_b - L0\right) + k_{yy}y_f - d_{yy}\dot{y}_b + d_{yy}\dot{y}_f + F_{Dy}\right) \\ \ddot{y}_f = -g + \dfrac{1}{m_f}\left(k_{yy}\left(y_b - L0\right) - k_{yy}y_f + d_{yy}\dot{y}_b - d_{yy}\dot{y}_f - k_{env}y_f - d_{env}\dot{y}_f - F_{Dy}\right) \end{cases} \tag{10}$$

In Eq. 10 y_b and y_f are the body and foot vertical displacements, $L0$ is the length of the leg when there is no foot spring compression, g is gravity, k_{yy} and d_{yy} are the end-effector stiffness and passive damping of the system in the y-direction, k_{env} and d_{env} are the stiffness and damping parameters in the ground model and F_{Dy} is the MR damper force projected in the y-direction.
During the flight phase the equation of motion is the one of 2 inertias connected with a spring-damper that floats under the effect of the gravity field:

$$\begin{cases} \ddot{y}_b = -g \\ \ddot{y}_f = -g + \dfrac{1}{m_f}\left[k_{yy}\left(y_b - L0 - y_f\right) + d_{yy}\left(\dot{y}_b - \dot{y}_f\right)\right] \end{cases} \tag{11}$$

In the model of the flight phase it has been assumed that due to the big difference in the masses of the body and the foot ($m_b >> m_f$) the reaction force coming from the foot can be neglected and only gravity is contributing to the body acceleration $\ddot{y}_b$.
In order to further simplify the model during stance phase in Eq. 10, a second order model has been considered that includes only the dynamics of the body mass. To perform this simplification it is necessary to understand if (with the actual physical parameters) the foot looses contact, after the impact with the ground, due to its own dynamics. Therefore a simulation of a 0.3 m drop test (on a very stiff ground surface ($K_{env}=10^6$ N/m) has been performed for two very different foot masses m_f (0.1 kg and 3.0 kg). The simulation results are presented in Fig. 11. The results show that the foot experiences a significant contact loss only in the case where the foot mass (unsprung mass) if very large (m_f = 3.0 kg). This is related to the fact that in that case the difference between the body mass and the foot unsprung mass is smaller. In the case of this study (m_f=0.1 kg) no contact loss has been predicted. Therefore, it is assumed that the contact loss between the foot tip and the ground is caused by the dynamics of the larger body mass and therefore the model of the leg can be simplified as:

$$\begin{cases} \ddot{y}_{b\ \ Flight} = -g \\ \ddot{y}_{b\ \ Stance} = -g + \dfrac{1}{m_b}\left(-k_{yy}\left(y_b - L0\right) + k_{yy}y_f - d_{yy}\dot{y}_b + d_{yy}\dot{y}_f + F_{Dy}\right) \end{cases} \tag{12}$$

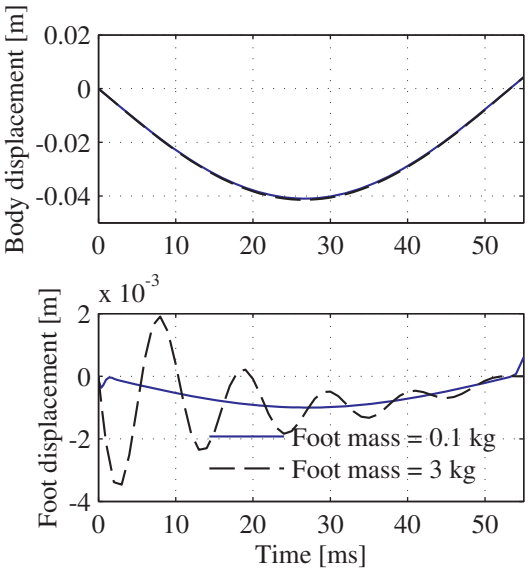

Fig. 11 Simulation of 0.3 m drop tests with m_f=3 kg (dashdot) and m_f=0.1 kg (solid): body displacement (1st plot) and foot displacement (2nd plot). The plot starts at the moment of touchdown.

7.2 Online stiffness identification

On-line identification is useful when the stiffness of the ground changes. By identifying the ground stiffness, the parameters of the controller can be adapted accordingly and the performance of the semi-active damping can be optimized. The basic idea of the online stiffness identification is that the natural frequency of the system does not change if the dynamics of the leg is described in the task space or in the joint space. However, the vertical position information of the slider encoder would not be available on a robot moving freely in the 3D space; a reliable estimate of the natural frequency can be obtained by using the measurements of the spring displacement. In this method the spring compression time Δt and the maximum spring compression is measured every time the legs lands on the ground. The measuring sequence is illustrated in Fig. 12.

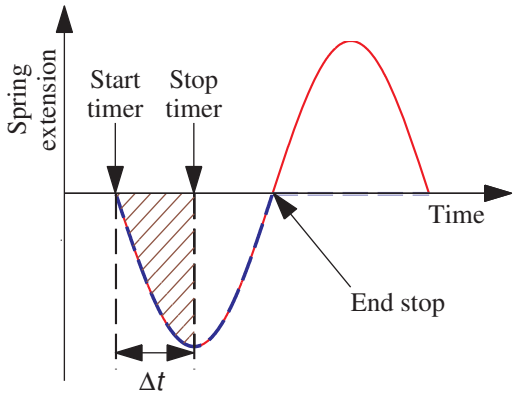

Fig. 12 Damped response of a second order spring-mass-damper system (solid), compression of the spring after the impact (dashed). Once the spring has recovered its rest length a mechanical end-stop prevents further extension

By roughly assuming that Δt is a fourth of the oscillation period of time T of the damped oscillatory response, the natural frequency of the damped system can be calculated as:

$$T = 4\Delta t \Rightarrow \omega_d = \frac{2\pi}{4\Delta t} = \sqrt{\omega_n^2 - \frac{d_{yy}}{4m_b^2}} \tag{13}$$

where ω_d is the angular frequency of the damped oscillation. If the body mass m_b and the damping d_{yy} is known (after earlier identification), the end-effector stiffness k_{yy} can be estimated by:

$$\omega_n = \sqrt{\frac{k_{yy}}{m_b}} \Rightarrow k_{yy} = \frac{d_{yy}^2}{4m_b} + \omega_r^2 m_b \tag{14}$$

Note that the k_{yy} stiffness includes also the ground stiffness. If the leg lands in a soft surface this ground compliance will be added in series to the foot reducing the overall compliance and resulting in lower forces that will build up for a longer time. This will result in a longer time Δt to decelerate completely the body mass and achieve the maximum leg compression. The outcome of this algorithm for estimating the stiffness by the compression time is a value that includes all the sources of compliance that can affect the mass dynamics (e.g. ground and joint stiffness) without having to estimate them separately. Furthermore the fact that the estimation is performed at each bouncing step enables the system to efficiently adapt to different ground surface stiffness.

8 CONTROL ALGORITHMS

The main goal of the control law, proposed in this section, is to eliminate the bouncing of the leg during the ground contact and therefore improve the traction between the foot tip and the ground. This consists essentially in dissipating the excess of energy (stored in the spring) that, once released, would create re-bouncing. A secondary goal can be to reduce the impact forces transmitted to the torso by semi-active control of the damping force.

8.1 Critical damping law

During the spring compression phase the control is not active and the compliance of the system is mainly determined by the passive spring and the ground compliance. It must be underlined that, during compression phase, any force created by the damper would be pointing upwards increasing the force transmitted to the robot body. In order to minimize the accelerations transmitted to the robot body, the controllable damping force is applied only during the elongation phase of the compliant foot. In consequence the controllable damping force will be always directed in the opposite direction to the spring force. In order to attain a critically damped response for the robotic leg, a control law is proposed (in the task space) whereby a damping force is controlled as a combination of a virtual negative spring and a virtual damping element. The damping force F_{Dy} (expressed in the vertical direction y), can be formulated as:

$$F_{Dy} = \alpha(y_b - L0) - \beta\dot{y}_b \tag{15}$$

where α is the negative spring constant and β is the virtual damping coefficient, while y_b-$L0$ represents the extension/compression of the leg in task space. Further on by combining Eq. 15 with Eq. 12 and using the notation defined in Fig. 10b, the vertical dynamics (given the constraint of the foot touching the ground $y_f = 0$) is described by:

$$\begin{aligned} &m_b\ddot{y}_b = -m_b g + (\alpha - k_{yy})(y_b - L0) + (-d_{yy} - \beta)\dot{y}_b \Rightarrow \\ &m_b\ddot{y}_b + (k_{yy} - \alpha)(y_b - L0) + (d_{yy} + \beta)\dot{y}_b = -m_b g \end{aligned} \tag{16}$$

In (Eq. 16) the end-effector stiffness k_{yy} can be estimated by the on-line identification during the antecedent compression phase, whereas d_{yy} is obtained by identification tests. To attain critically damped response the controller has two degrees of freedom α and β to be set. The influence of these parameters on the damped natural frequency ω_d and on the damping factor ξ of the system is described by Eq. 17. The parameter α can be chosen according to the desired settling time. A higher

value of α will result in a more compliant leg and this will also reduce the forces transmitted to the torso because the energy stored in the spring is dissipated in a longer time interval. On the other hand, if the goal is to damp the oscillation in shorter time, a lower value of α must be set. The parameter β must be set accordingly (see Eq. 17) to obtain a critically damped response ($\xi=1$) and so no over-bounce should occur.

$$\omega_n = \sqrt{\frac{k_{yy} - \alpha}{m_b}} \quad \xi_{crit} = \frac{\beta + d_{yy}}{2m_b\omega_n} = \frac{\beta + d_{yy}}{2\sqrt{m_b\left(k_{yy} - \alpha\right)}} \tag{17}$$

The parameters α, β in Eq. 17 are defined in the end-effector space and must be mapped into the joint space because the controllable damping force F_{Di} is expressed along the foot joint q_3. This mapping makes use of the Jacobian, inverting Eq. 9:

$$A_j = J^T \begin{bmatrix} 0 & 0 \\ 0 & \alpha \end{bmatrix} J \quad B_j = J^T \begin{bmatrix} 0 & 0 \\ 0 & \beta \end{bmatrix} J \quad \alpha_j = A_{j(3,3)} \quad \beta_j = B_{j(3,3)}$$
$$F_{Dj} = \alpha_j q_3 - \beta_j \dot{q}_3 \tag{18}$$

where F_{Dj}, α_j and β_j are the controllable damping force and control parameters expressed in the joint space and q_3 and $\dot{q}_3$ are the foot spring displacement and velocity respectively. To generate F_{Dj} electric current must be driven in the coil of the MR damper according to the damper force characteristic depicted in Fig. 7.

9 EXPERIMENTAL RESULTS

This section presents experimental results of the ground stiffness and damping identification, and the responses of the critical damping control law for different values α of the negative spring.

During the elongation phase of the compliant foot, the total damping force must be always lower than the spring force to prevent that the elongation does not stop before the maximum extension of the foot spring. This suggests the convenience to express α as a fraction of the k_{yy} stiffness according to Eq. 19 by introducing the k_{ratio} variable:

$$\alpha = \frac{k_{ratio} k_{yy}}{100} \tag{19}$$

9.1 Stiffness and damping identification

The stiffness k_{yy} and passive damping d_{yy} of the system in y direction were identified by doing dropping tests when the controller was not active (only passive damping was present). In tests the leg was dropped from a height of 0.3 m on a very stiff ground in which case it was assumed that no compliance was added from the environment. Equation 12 was fitted to the measured data in order to estimate the stiffness and passive damping parameters. The results of the identification are plotted in Fig. 13 in which the slider displacement zero-level corresponds to the height of the slider when the foot is fully extended and the tip of the foot touches the ground. The identified parameters are k_{yy}=19000 N/m and d_{yy}=226 N/(m/s) which are further on used in the implementation of the control law.

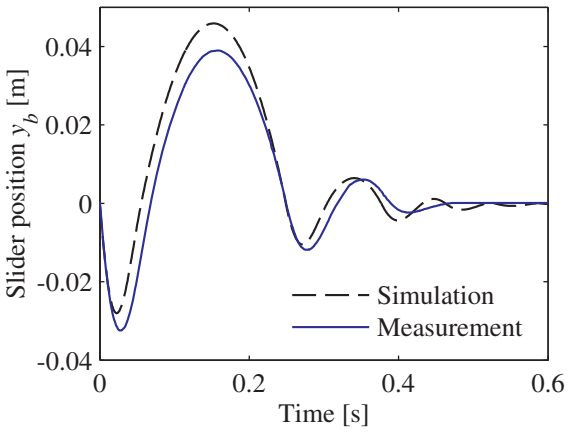

Fig. 13 Drop test (0.3m) for identification of kyy and dyy. Simulation with the identified parameters (solid) and experiments (dashdot)

Figure 13 shows that without any control action the leg bounces three times with a maximum bounce of 40 mm when the leg is dropped from the height of 0.3 m.

9.2 Results of the critical damping law

The effectiveness of the proposed control law was studied by dropping the leg from the heights of 0.1 m, 0.2 m and 0.3 m. The tests were performed with different values of the parameter k_{ratio}. The slider displacement y_b and the virtual damping force F_D responses were acquired. The results of the three drop heights are shown in Figs. 14, 15 and 16 respectively. In all figures the slider displacement zero -level corresponds to the level of the ground and the time line starts at the moment of touchdown.

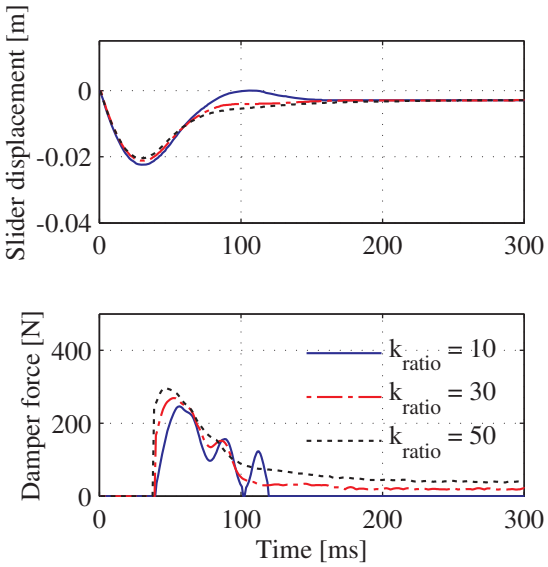

Fig. 14 Critical damping law for a 0.1 m drop test - k_{ratio}=10 (solid), 30 (dashdot), 50 (dotted): 1st plot slider displacement, 2nd plot damper force

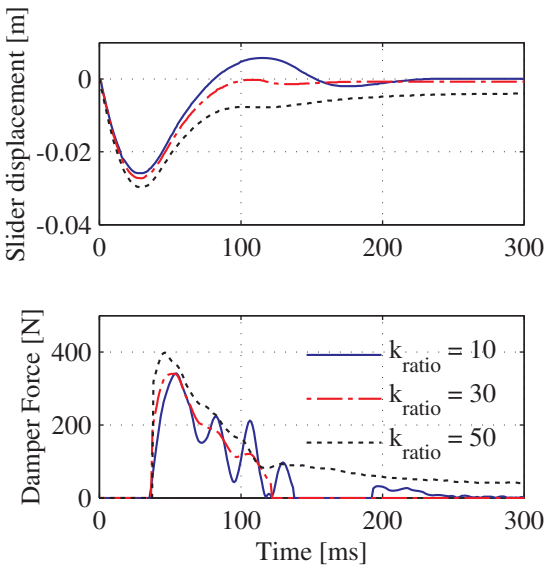

Fig. 15 Critical damping law for a 0.2 m drop test - k_{ratio}=10 (solid), 30 (dashdot), 50 (dotted): 1st plot slider displacement, 2nd plot damper force

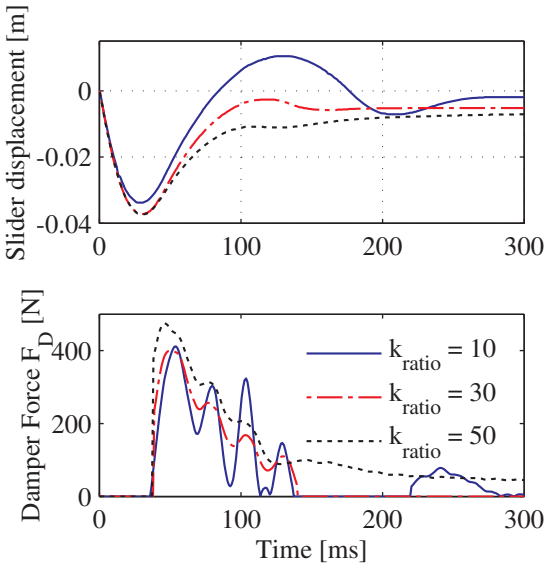

Fig. 16 Critical damping law for a 0.3 m drop test - k_{ratio}=10 (solid), 30 (dashdot), 50 (dotted): 1st plot slider displacement, 2nd plot damper force

The performance indexes used to evaluate the control law are the percent bounce reduction *%BR* and the settling time t_s. The first criteria is defined as the percent ratio between the overshoot with regard to the steady settling value, and the second criteria is defined as the time elapsed from the instant of maximum compression to the instant in which 99% of the steady settling value is reached. For example with k_{ratio}= 0 there is no virtual spring effect but only virtual damping and a bounce of 0.01 m for 0.3 m drop was achieved. This corresponds to a bounce reduction of 63%. With k_{ratio}=30 and k_{ratio}=50 results are better, as shown in Table 2 that lists and compares the performance of the above mentioned experiments.

Table 2, Bouncing reduction performance for different values of k_{ratio}

	Drop height [m]	Critical damping law		
Parameter		k_{ratio} 0	30	50
% BR	0.1	81	100	99
t_s [ms]		230	180	215
% BR	0.2	78	98	99
t_s [ms]		230	170	280
% BR	0.3	63	92	99
t_s [ms]		260	180	250

Table 2 shows that k_{ratio}=50 achieves the best performance in terms of bounce reduction for every drop height (99%) was achieved, but on the other hand, a higher k_{ratio} causes higher settling time that varies from 215 ms to 280 ms. The average settling time t_s is approximately 175 ms and 250 ms for k_{ratio}=30 and k_{ratio}=50 respectively. As expected a higher k_{ratio} results in higher α values and so higher settling times. Theoretically, settling time for an oscillatory system is independent of the dropping height and can be estimated as $t_s=4.6/\omega_n\xi$ [29]. Calculating ω_n by (14) the settling time should be 110 ms and 130 ms for k_{ratio}=30 and k_{ratio}=50 respectively and this fits with the experimental results in Fig. 18 (upper plot). Within the performed set of experiments, the best trade-off between settling time and bounce reduction was obtained with k_{ratio}=30.
Since the critical damping law was applied only during the extension phase of the compliant foot, it is clear that the maximum force transmitted to the torso depends only on the drop height of the leg and therefore on the maximum spring compression. To remove more energy in a shorter period of time a variant of the critical damping law could be implemented, in which a damping force is also generated during the compression phase thus leading to a smaller maximal compression. In this modification the damping force during the compression phase could be implemented as a constant force or as a force that is proportional to the compression speed and position of the compliant foot. However, if the goal is to reduce the accelerations of the torso and make the ground contact and compression phase of the compliant foot as smooth as possible, it is not convenient to use this modified control strategy. Furthermore, an on-line estimation of the stiffness is always preferable during the compression phase.

10 CONCLUSIONS

This paper presented the design, model and experimental evaluation of the performance of a novel compliant foot for the feet of a quadruped robot. The compliance of the robotic foot was carried out by a linear spring and magnetorheological technology was used to integrate a semi-active damper into the foot construction. Utilization of MR fluids enables real-time control of the damping force during single ground contact in which case the traction of the foot can be improved.
The performance of the MR damper was analyzed from the static and dynamic point of view and a third order analytic model of the MR damper was found to fit to the static characteristic curve with a good correlation between the model and measured data. As a static performance the damping force was able to be altered in a range of 15 N to 310 N at low velocities and at the maximum measured speed of 60 mm/s the dynamic range was calculated to be 14.9. The achieved dynamic range can be considered as an indication of the controllability of the damping force in a wide range and a successful value within this application.

The dynamic performance of the damper was studied by using sinusoidal excitation to define the operating bandwidth of the MR damper. As a result the -3 dB level of the damping force was found beyond 100 Hz proving the damper can be used in real-time control applications.
In the control application the performance of the magnetorheological compliant foot was estimated by drop-down experiments. In the drop-down experiments the robotic leg with the compliant foot was fixed on a vertically sliding test setup that allowed one degree of freedom movement for the leg and reproducible circumstances for the tests. The aim of these experiments was to study how the chatter between the foot tip and the ground could be avoided by integrating a semi-active damping element into the compliant foot of a robotic leg. A control law (critical damping law) has been proposed whereby the damping force of compliant foot is controlled as a combination of a negative spring and a virtual damping element.
The aim was to dissipate all the kinetic energy during the first ground contact sequence. As feedback information for the control laws only the spring compression in the compliant foot was used. This enabled the real-time control of the damping force of the magnetorheological compliant foot. Furthermore an online algorithm was proposed with the purpose to identify the end-effector stiffness (including the environmental surface stiffness) during the compression phase. This made the system able to adapt to different ground surfaces, on which the robot moves. By online identification the implemented controller parameters can be actively tuned based on the total mass of the robot and the identified leg stiffness.
The performances of the control law for different dropping heights was assessed by experimental tests using bounce reduction *%BR* and settling time t_s as performance criteria. The best trade-off between the settling time and the bounce reduction was found with K_{ratio}=30 when 98 %BR and 170 ms settling time can be achieved with medium drop height of 0.2 m.
Future works will consider the test of the effectiveness of the proposed approach with the hydraulic cylinders mounted on the leg. In that case the hydraulic compliance will have to be included in the joint stiffness matrix and will affect the leg compliance. However, the stiffness identification algorithm will not change and its outcome will include also this additional source of compliance. In addition, the constraint of the leg mounted on a vertical slider will be relaxed, considering the leg landing with different angles and postures. The use of an IMU (inertial measurement unit) in conjunction with the joint encoders will tell the position of the leg joints in a world frame. An appropriate Jacobian (that will include the body posture) will map the joint movements to the end-effector movements (defined in the world frame) allowing the implementation of the proposed control law without any loss of generality.
Performance with different surfaces may be also investigated. Furthermore four new magnetorheological compliant foots which are optimized for the HyQ robot, will be designed and manufactured in order to be able to study the semi-active compliance during walking and running.

11 ACKNOWLEDGMENT

The work was funded by the Fondazione Istituto Italiano di Tecnologia and Tekes – the Finnish Funding Agency for Technology and Innovation.

REFERENCES

[1] D. W. Robinson, J. E. Pratt, D. J. Paluska and G. A. Pratt, 1999, “Series Elastic Actuator Development for a Biomimetic Walking Robot,” *Proc. IEEE/ASME International Conference on Advanced Intelligent Mechatronics,* pp. 561–568

[2] J. Buchli, M. Kalakrishnan, M. Mistry, P. Pastor, and S. Schaal, 2009, "Compliant Quadruped Locomotion over Rough Terrain," *Proc. IEEE/RSJ International Conference on Intelligent Robots and Systems (IROS)*, pp. 814–820.

[3] J. E. Pratt and B. T. Krupp, 2004, "Series Elastic Actuators for Legged Robots," *Proc. SPIE – The International Society for Optical Engineering*, **5422**, pp. 135–144.

[4] G. A. Pratt and M. M. Williamson, 1995, "Series Elastic Actuators," *Proc. IEEE – Int. Workshop on Intelligent Robots and Systems (IROS'95)*, pp. 399–406.

[5] G. Tonietti, R. Schiavi, and A. Bicchi, 2005, "Design and Control of a Variable Stiffness Actuator for Safe and Fast Physical Human/Robot Interaction," *Proc. IEEE – Int. Conf. Robotics and Automation (ICRA'05)*, pp. 526–531.

[6] J. W. Hurst, J. Chestnutt, and A. Rizzi, 2004, "An Actuator with Mechanically Adjustable Series Compliance," Carnegie Mellon Robotics Institute, Technical report, (available at http://www.ri.cmu.edu/pub_files/pub4/hurst_jonathan_w_2004_1/hurst_jonathan_w_2004_1.pdf)

[7] C. –P. Chou and B. Hannaford, 1996, "Measurement and Modeling of McKibben Pneumatic Artificial Muscles," *IEEE Trans. Robotics and Automation*, **12**(1), pp. 90–102.

[8] B. Verrelst, R. Van Ham, B. Vanderborght, F. Daerden, and D. Lefeber, 2005, "The Pneumatic Biped LUCY Actuated with Pleated Pneumatic Artificial Muscles," *Autonomous Robots*, **18**(13), pp. 201–213.

[9] Klute GK, Czerniecki JM and Hannaford B, 2002, "Artificial Muscles: Actuators for Biorobotic Systems," *The International Journal of Robotics Research*, **21**(4), pp. 295–309.

[10] K. W. Wait and M. Goldfarb, 2010, "Enhanced Performance and Stability in Pneumatic Servosystems With Supplemental Mechanical Damping," *Journal of Dynamic Systems,M easurement, and Control*, **132**(4).

[11] K. W. Wait and M. Goldfarb, 2011, "Design and Control of a Pneumatic Quadrupedal Walking Robot," *IEEE International Conference on Robotics and Automation (ICRA)*, pp.587–592.

[12] C. Chee–Meng, H. Geok–Soon and Z. Wei, 2004, "Series Damper Actuator: a Novel Force/Torque Control Actuator," *4th IEEE/RAS International Conference on Humanoid Robots*, pp. 533-546.

[13] M. Laffranchi, N. Tsagarakis, and D. Caldwell, 2010, "A Variable Physical Damping Actuator (VDPA) for Compliant Robotic Joints," *IEEE International Conference on Robotics and Automation (ICRA)*, pp. 1668–1674.

[14] C. Semini, N. G. Tsagarakis, E. Guglielmino, M. Focchi, F. Cannella and D. G. Caldwell, 2011, "Design of HyQ - a Hydraulically and Electrically Actuated Quadruped Robot," *Journal of Systems and Control Engineering*, **225**(6), pp. 831–849.

[15] C. Semini, 2010, "HyQ - Design and Development of a Hydraulically Actuated Quadruped Robot," Italian Institute of Technology and University of Genoa, Ph.D. thesis.

[16] N. Jalili, 2002, “A Comparative Study and Analysis of Semi-Active Vibration-Control Systems,” *Journal of Vibration and Acoustics*, **124**(4), pp. 593–605.

[17] G. Bossis, S. Lacis, A. Meunier and O. Volkova, 2002, “Magnetorheological Fluids,” *Journal of Magnetism and Magnetic Materials,* **252**, pp. 224–228.

[18] F. D. Goncalves, M. Ahmadian and J. D. Carlson, 2006, “Investigating the Magnetorheological Effect at High Flow Velocities”, *Smart Materials and Structures*, **15**(1), pp. 75–85.

[19] J. Kostamo, E. Kostamo, J. Kajaste and M. Pietola, 2008, “Magnetorheological (MR) Damper with a Fast Response Time”, *Proc. FPMC 2008,* pp. 169–182.

[20] Lord Corporation*,* 2009, “Magnetorheological Fluid MRF132DG,” Product specification.

[21] G. Yang, B. F. Spencer, J. D. Carlson and M. K. Sain, 2002, “Large Scale MR Fluid Dampers: Modeling and Dynamic Performance Considerations,” *Engineering Structures,* **24**(3), pp. 309–323.

[22] N. D. Sims, R. Stanway, D. J. Peel, W. A. Bullough and A. R. Johnson, 1999, “Controllable Viscous Damping: an Experimental Study of an Electrorheological Long Stroke Damper under Proportional Feedback Control,” *Smart Materials and Structures,* **8**(5), pp. 601–615.

[23] H. Kauranne, J. Kajaste and M. Vilenius, 2004, *Hydraulitekniikan Perusteet*, pp. 48.

[24] M. Mao, W.H. Young-Tai and N.M. Wereley, 2007, “A Magnetorheological Damper with Bifold Valves for Shock and Vibration Mitigation,” *Jounal of Intelligen Material Systems and Structures*, **18**, pp. 1227–1232.

[25] B.J. Bass and R.E. Christenson, 2007, “System Identification of a 200 kN Magneto-Rheological Fluid Damper for Structural Control in Large-Scale Smart Structures,” *Proc. American Control Conference*, pp. 2690–2695

[26] Q.-H. Nguyen and S.-B.Choi, 2009, “Optimal Design of a Vehicle Magnetorheological Damper Considering the Damping Force and Dynamic Range,” Journal of Smart Materials and Structures, **18**(1), pp. 1–10.

[27] B. Siciliano, L. Sciavicco, L. Villani and G. Oriolo, 2009, *Robotics Modelling, Planning and Control*, Springer.

[28] J. McIntyre, F.A. Mussa-Ivaldi, E. Bizzi and J. McIntyre, 1996, “The Control of Stable Postures in the Multi–Joint Arm”, *Experimental Brain Research*, **110**, pp. 248–264.

[29] A. Hemami and G. Zeng, 1997, “An Overview of Robot Force Control,” *Robotica*, **15**(5), pp. 473–482.